MRS Communications (2014), *4*, 31–44
© Materials Research Society, 2014
doi:10.1557/mrc.2014.13

MRS Communications

Prospective Articles

Self-assembled vertical heteroepitaxial nanostructures: from growth to functionalities

Heng-Jui Liu, Wen-I Liang, and **Ying-Hao Chu,** Department of Materials Science and Engineering, National Chiao Tung University, Hsinchu 30010, Taiwan
Haimei Zheng, Materials Sciences Division, Lawrence Berkeley National Laboratory, Berkeley, California 94720
Ramamoorthy Ramesh, Department of Materials Science and Engineering, University of California, Berkeley, California 94720
Address all correspondence to Ying-Hao Chu at **yhc@cc.nctu.edu.tw**

(Received 24 December 2013; accepted 17 April 2014)

Abstract

Self-assembled vertical heteroepitaxial nanostructures (VHN) in the complex oxide field have fascinated scientists for decades because they provide degrees of freedom to explore in condensed matter physics and design-coupled multifunctionlities. Recently, of particular interest is the perovskite-spinel-based VHN, covering a wide spectrum of promising applications. In this review, fabrication of VHN, their growth mechanism, control, and resulting novel multifunctionalities are discussed thoroughly, providing researchers a comprehensive blueprint to construct promising VHN. Following the fabrication section, the state-of-the-art design concepts for multifunctionalities are proposed and reviewed by suitable examples. By summarizing the outlook of this field, we are excitedly expecting this field to rise with significant contributions ranging from scientific value to practical applications in the foreseeable future.

Introduction

In the past decades, self-assembled nanocomposites have become a glamorous research topic because various kinds of fascinating and novel properties and multifunctionalities can be designed *via* the intercoupling among spin, orbital, charge, and lattice degrees of freedom within the materials.[1–3] Notably in the research field of complex oxides, the applicable functionalities for combination cover almost all application spectra, ranging from metallic, semiconducting, insulating, ferromagnetic, ferroelectric, multiferroic, superconducting, nonlinear optical effects, etc.[4] In addition, an important factor that affects the functionalities of composites is the connectivity, defined as the number of dimensions in which the components are self-connected. The possible connectivities can be sorted out in 16 different types: 0–0, 1–0, 2–0, 3–0, 1–1, 2–1, 3–1, 2–2, 3–2, 3–3, 0–1, 0–2, 0–3, 1–2, 1–3, and 2–3. However, the most common schemes, 0–3-type particulate composites, 2–2-type laminate composites, and 1–3-type fiber composites, are able to give rise to the specific anisotropic properties.[2,5] With the recent advancements in thin-film processes, the self-assembled composites can also be fabricated at nanoscale in a film-on-substrate geometry. Comparing with 2–2-type multilayer films, 1–3-type nanocomposite thin films draw more attention because of the high interface-to-volume ratio and intriguing physical properties. The first successful demonstration of such nanocomposite is the $(La_{0.67}Ca_{0.33}MnO_3)_{1-x}$–$(MgO)_x$ composite system on a (100)-oriented MgO substrate by means of the metal organic aerosol deposition method, by Lebedev et al. in 2002.[6] When the concentration of MgO exceeds 0.3 ($x > 0.3$), $La_{0.67}Ca_{0.33}MnO_3$ grains are separated and surrounded by the MgO matrix. A latter work by Moshnyaga et al.[7] also confirmed that the structural and magnetotransport properties of the $La_{0.67}Ca_{0.33}MnO_3$ nanoclusters can be tuned by the tensile stress originating from the MgO second phase. Nevertheless, one of the most studied systems, recently, is the nanocomposite thin films consisting of perovskite and spinel materials, starting from the pioneering work of spinel $CoFe_2O_4$ nanopillars embedded in perovskite $BaTiO_3$ grown on the (001)-oriented $SrTiO_3$ substrate.[8–10] This system exhibits an enhanced and controllable magnetoelectric (ME) coupling, wherein the magnetic property of the nanocomposites can be manipulated by applying an electric field and vice versa. In addition, controllability of intriguing functionalities, such as the enhanced low-field magnetoresistance (LFMR) in $(La_{0.7}Sr_{0.3}MnO_3)_{0.5}$–$(ZnO)_{0.5}$ vertically aligned nanocomposite (VAN) thin films,[11] the improved dielectric response in $(BiFeO_3)_{0.5}$–$(Sm_2O_3)_{0.5}$[12] and the enhanced ferroelectricity in $(BaTiO_3)_{0.5} - (Sm_2O_3)_{0.5}$[13] self-assembled vertical heteroepitaxial nanostructures (VHNs), are continuously unveiled. In this review, we emphasize on the development of 1–3-type nanocomposite thin films, or the so-called "self-assembled VHN thin films", in particular, the systems composed of perovskites and spinels. In the following section, we will first introduce the fabrication of the self-assembled VHN films by the pulsed laser deposition (PLD) process and the corresponding growth mechanisms, which are extensively studied

https://doi.org/10.1557/mrc.2014.13 Published online by Cambridge University Press

recently. Growth parameters such as temperature, substrate orientation, and strain are very crucial in determining the morphologies and crystal anisotropies of nanocomposites. As the main objective of the growing VHN is to be able to explore the multi-functionalities, we will introduce the approaches to functionality design by three dominant interactions—mechanical, physical, and chemical—case by case along with several recent works that include phenomena such as the ME effect, photomagnetic effect, large magnetoresistance (MR), etc. In the final section, the conclusive concepts will be delineated again and the future directions will be suggested. We genuinely hope that this comprehensive review from growth to design of the nanomaterial systems provide readers an opportunity to understand the magnificence of VHN and further helps to develop innovative designs with the desired properties for practical applications in the future era.

Growth mechanism of self-assembled VHN

Fabrication of the self-assembled VHN films has been successfully synthesized via several techniques such as PLD,[9,11,14–16] pulsed electron deposition (PED),[17] and chemical solution method.[6,7,18] The main fabrication method focused in this paper is the PLD process. PLD has many advantages, such as precise stoichiometry transfer from target to substrate, fast growth rate, high crystalline quality of film, and versatility of growing a wide range of complex materials, and thus it becomes the most popular tool to develop the nanostructure systems.

The schematics in Fig. 1(a) visually describe the general evolution of self-assembled VHN films consisting of two constituents with different structures from initial to final stages. These selected materials are almost immiscible with each other that can result in spontaneous phase separation. In the very early stage of deposition before the substrate being fully covered with the deposited constituents, the material with higher wetting ability prefers to form lamellas or nanosheets (layer-by-layer growth mode) and the other in less contact with the substrate would form nanoparticles (island growth mode). As these species continue to arrive onto the substrate from target, the material with the layer-by-layer growth mode quickly fills the empty space and limits the growth direction of the nanocrystals along the out-of-plane direction. Finally, the film after the growth exhibits the self-assembled nanostructured thin film with 1–3 phase interconnectivity. This growth dynamics of the self-assembled VHN has been evidenced in the famous example of $BiFeO_3$–$CoFe_2O_4$ composites, reported by Zheng et al.[8] and Hsieh et al.[19] Based on the Winterbottom construction, the $CoFe_2O_4$ deposited on the (001)-oriented $SrTiO_3$ substrate has weaker wetting ability than $BiFeO_3$, which leads to the island growth mode for $CoFe_2O_4$ and the layer-by-layer mode for $BiFeO_3$.[10] The in situ reflective high-energy electron diffraction (RHEED) patterns in Fig. 1(b) show the evolution of $CoFe_2O_4$ nanocrystals, with increasing laser pulses from 0 to 18,000, on the (001)-oriented $SrTiO_3$ substrate at 700 °C. The typical diffraction spots of $CoFe_2O_4$ nanocrystals, as emphasized by red circles, emerge with weakened streak feature of the $SrTiO_3$ substrate at very early stage of the PLD process about 100–150 pulses, and the mean size of about 8 nm $CoFe_2O_4$ particles can be observed on the surface as shown in atomic force microscopy (AFM) images [Fig. 1(c)]. As the deposition process goes on to 18,000 pulses, only the diffraction feature of the $CoFe_2O_4$ remains on the RHEED screen. It indicates that $CoFe_2O_4$ nanocrystals congregate to become nanopillars embedded in $BiFeO_3$ matrix, and present the morphology of extrusive truncated pyramids that is the equilibrium shape of $CoFe_2O_4$ crystal with eight {111} facets [Fig. 1(d)]. The similar observation has been made

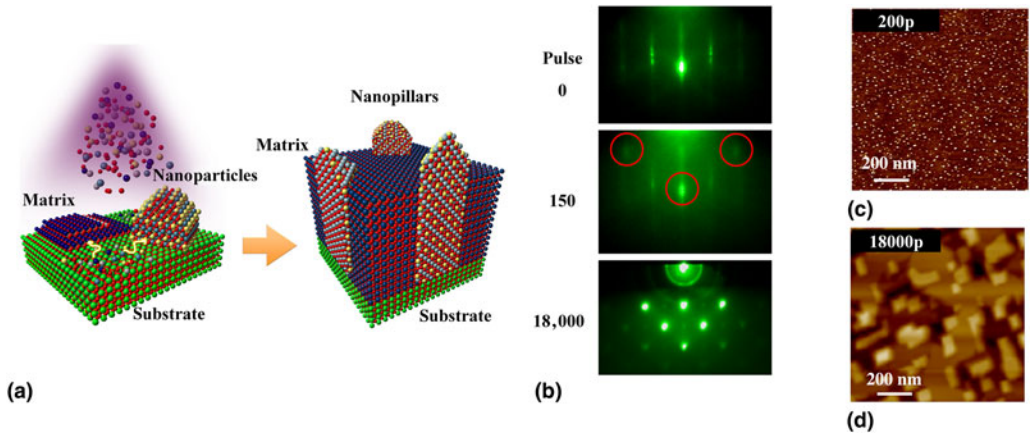


Figure 1. (a) Schematic evolution of self-assembled VHN films from initial to final stage. (b) The evolution of $CoFe_2O_4$ nanostructures on the $SrTiO_3$ substrate at 700 °C recorded by RHEED patterns with counts of laser pulse from 0 to 18,000. (c) AFM images of $CoFe_2O_4$ nanocrystals in 8 nm of mean size (700 °C, 200 pulses). (d) AFM images of $CoFe_2O_4$ nanopillars, showing the morphology of extrusive truncated pyramids (700 °C, 18,000 pulses). (b), (c), and (d) are reproduced from Ref. 19 by permission of The Royal Society of Chemistry.

https://doi.org/10.1557/mrc.2014.13 Published online by Cambridge University Press

in the case of $SrRuO_3$–$CoFe_2O_4$ system using dual targets PLD process proposed by Liu et al.[15]

Control of nanostructure: size, morphological shape, and crystallographic orientation

Effect of temperature on the size of nanostructures

Substrate temperate is an important parameter to control the mean size of self-assembled nanostructures in two-phase composite thin films. Results in Figs. 2(a) and 2(b) obtained from Zheng et al.[8] and Hsieh et al.[19], respectively, indicate that the formation of the self-assembled nanostructures follows the heterogeneous nucleation and growth theory well. In the initial stage of deposition, the ultrafine crystals can be seen as nuclei and the respective critical radius in the classical nucleation theory is obtained as[20]

$$r^* = -\frac{2\gamma_{12}}{\Delta G_{het}} = \left(\frac{2\gamma_{12}}{\Delta H_{het}}\right)\frac{T_m}{T_m - T_s} = \left(\frac{2\gamma_{12}T_m}{\Delta H_{het}}\right)\frac{1}{1 - T_s/T_m}, \quad (1)$$

where γ_{12} is the interfacial energy between the substrate and $CoFe_2O_4$ nuclei; ΔG_{het} and ΔH_{het} are the change in free-energy barrier and enthalpy per unit volume for heterogeneous nucleation, respectively; T_m is the melting point of $CoFe_2O_4$ (1843 K),[21] and T_S is the surrounding temperature (or substrate temperature). For a small variation of T_S/T_m (from 0.466 at 600 °C to 0.519 at 700 °C), the critical radius of nuclei is expected to follow an approximately linear dependence with temperature, which is consistent with the results in Fig. 2(a). As the deposition continues, the nuclei that exceed the critical size start to grow, and the crystal size is determined by movement of atoms, which can better be described by the standard two-dimensional (2D) diffusion model[8]:

$$d^2 = 4\tilde{D}_0\, e^{-E_a/kT} t = 4\tilde{D}_0\, e^{-E_a/kT}\frac{1}{\nu}, \quad (2)$$

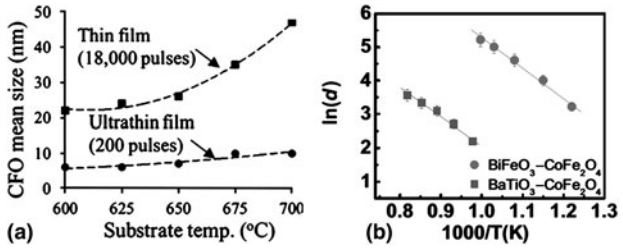


Figure 2. (a) Relationships of $CoFe_2O_4$ mean size and substrate temperature for thin film (18,000 pulses) and ultrathin film (200 pulses). Reproduced from Ref. 19 by permission of The Royal Society of Chemistry. (b) Temperature dependence of $BiFeO_3$–$CoFe_2O_4$ and $BaTiO_3$–$CoFe_2O_4$ nanostructures grown on (001)-oriented $SrTiO_3$ substrates. Reproduced from Ref. 8 by permission of © 2006 WILEY–VCH Verlag GmbH & Co. KGaA, Weinheim.

where d is the lateral size; is the maximum value of the diffusion constant at infinite temperature; E_a is the activation energy; k is the Boltzmann constant; T is the temperature, and t is the diffusion time. Since diffusion is finite within the sample during the deposition, the diffusion time is thus determined by the growth rate ($\nu = 1/t$). The equation can then be simplified as

$$\ln d = A - B\frac{1}{T}, \quad (3)$$

where A and B are constants, and $B = E_a/2k$. It clearly demonstrates that in steady state the pillar diameter exponentially increases with the substrate temperature, which is consistent with the observed results as shown in Fig. 2(b). Based on these results, we are aware that the formation of nanopillars obeys the theory of nucleation and growth wherein the substrate temperature is a dominant parameter to determine the diffusivity and the final size thereof.

In addition, the post-annealing process also has significant influence on the diffusion behavior. Yan et al. have proposed that the diffusion behavior would change from two dimensions to preferably one dimension when the annealing temperature increases to ~1060 °C in $BaTiO_3$–$CoFe_2O_4$ nanocomposite.[22,23] When the annealing temperature is high enough (>980 °C), these spinel nanopillars merge into larger ones at the expense of smaller ones and in some regions the belt-shaped nanostructures elongated along the <110> direction appear. Such a high temperature lessens the clamping effect of the substrate and matrix on $CoFe_2O_4$, and the results in the fact that $CoFe_2O_4$ prefers a ledge growth mechanism, similar to the original growth of spinel single crystal due to a spatial distribution of cations along the <110> direction.

Tailoring morphology and crystallographic anisotropy of the nanostructures by substrate engineering

Formation of nanostructures of different sizes can be thought as the consequence of diffusion mechanism, in addition, the morphologies and crystallographic anisotropy can be manipulated by connectivity among the deposited species and substrates, and energetic competition between the respective surfaces and interfaces. According to the Winterbottom construction, at equilibrium, the competition among different surface energy terms dictates the shape and the ability of a particular material to form the nanostructure in the matrix of other material. One of the representative examples is $BiFeO_3$–$CoFe_2O_4$ VHN grown on different orientations of $SrTiO_3$ substrates, as shown in Fig. 3.[8,10] Usually, the lowest surface energy in most of the perovskite phases lies on {100} planes, and thus it leads to a cubic equilibrium shape with six {100} facets. In contrast to perovskites, spinels have the lowest surface energy on {111} surfaces, reflected in an equilibrium shape of an octahedron bounded by eight {111} facets. Therefore, on a (001) $SrTiO_3$-oriented substrate, $BiFeO_3$ wets the substrate

https://doi.org/10.1557/mrc.2014.13 Published online by Cambridge University Press

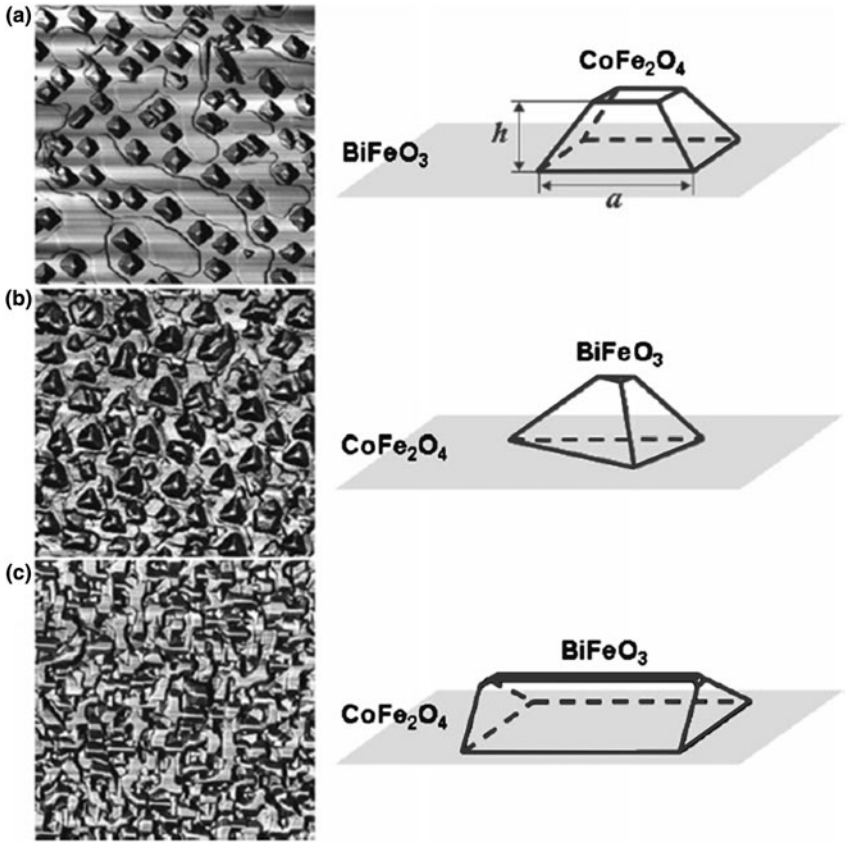


Figure 3. AFM phase-contrast images of $BiFeO_3$–$CoFe_2O_4$ nanostructures (volume fraction of 1:1) grown on (a) (001)-, (b) (111)-, and (c) (110)-oriented $SrTiO_3$ substrates. All images are 2.5 μm × 2.5 μm. The schematics show the shape and facets of the islands. On the (001) substrate, $CoFe_2O_4$ has a (001) end facet and (111), $(1\bar{1}1)$, $(\bar{1}11)$, and $(\bar{1}\bar{1}1)$ side facets. On the (111) substrate, $BiFeO_3$ has a (111) end facet and (001), (010), and (100) side facets. On the (110) substrate, $BiFeO_3$ has a (110) top end facet and (001), (010), $(00\bar{1})$, and (100) side facets. Reproduced from Ref. 8 by permission of © 2006 WILEY-VCH Verlag GmbH & Co. KGaA, Weinheim.

completely and $CoFe_2O_4$ prefers islands bonded by four {111} surfaces in the nucleation stage. As the growth process continues, $CoFe_2O_4$ will grow as pillars embedded in a $BiFeO_3$ matrix, which remain the morphology of extrusive pyramids on surface. Conversely, on the (111)-oriented $SrTiO_3$ substrates, $CoFe_2O_4$ has more wetting ability than $BiFeO_3$, where $BiFeO_3$ becomes the nanopillars embedded in a $CoFe_2O_4$ matrix and the corresponding morphology presents $BiFeO_3$ tetrahedrons with a small (111) end facet on its top and (001), (010), and (100) side facets. On the (110)-oriented $SrTiO_3$ substrate, the wetting abilities of both $BiFeO_3$ and $CoFe_2O_4$ phases are close that results in formation of a maze pattern. In this case, $BiFeO_3$ still has a higher surface morphology than $CoFe_2O_4$ and forms hut-shaped islands with the (110) end facet and the {100} side facets. Similar conclusion can be drawn in case of the $BiFeO_3$–$CoFe_2O_4$ nanocomposites grown on the (001)-oriented $MgAl_2O_4$ substrate as proposed by Stern et al. Their result shows that the spinel $CoFe_2O_4$ has higher wetting ability than perovskite $BiFeO_3$, and perovskite $BiFeO_3$ becomes nanogrids surrounded by spinel $CoFe_2O_4$, while these two materials are deposited on the spinel $MgAl_2O_4$ substrate.[24] In these samples, $BiFeO_3$ and $CoFe_2O_4$ have the same crystallographic orientation with respect to the orientation of the $SrTiO_3$ substrate, which is a cube-on-cube type of epitaxial relationship. It indicates that the morphological shapes are highly correlated to the crystallographic orientation.

The phase fraction of spinel (x) is another crucial parameter for the morphologies of nanocomposite thin films as well. The same ratio at different pervoskite matrices may lead to different results. Zheng et al.[8,25] and Levin et al.[25] have demonstrated the morphological changes on several phase fractions in $BiFeO_3$–$CoFe_2O_4$ and $PbTiO_3$–$CoFe_2O_4$ systems, respectively. As shown in Figs. 4(a) and 4(b), both the systems grown on the (001) $SrTiO_3$ substrate have less change of morphology as the phase fraction varies from 1/3 to 2/3, and $CoFe_2O_4$ still remains as the nearly original nanopillars form in either $BiFeO_3$ or $PbTiO_3$ matrix. However, marked discrepancies can be observed between these two systems on (110) and (111) substrates when the phase fraction reverses from 1/3 to 2/3. The morphology of $PbTiO_3$–$CoFe_2O_4$ at $x = 1/3$ starts as an alternating vertical lamellae and labyrinth-like shape while grown on

https://doi.org/10.1557/mrc.2014.13 Published online by Cambridge University Press

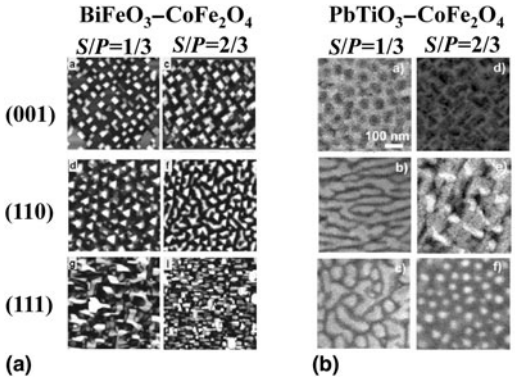


Figure 4. (a) AFM images of (x) $CoFe_2O_4$–($1-x$) $BiFeO_3$ nanostructures with $x = 1/3$ and 2/3 grown on (001), (111), and (110) $SrTiO_3$ substrates. All images are 3 μm × 3 μm. Reproduced from Ref. 8 by permission of © 2006 WILEY–VCH Verlag GmbH & Co. KGaA, Weinheim (b) SEM images revealing the morphologies of the (x) $CoFe_2O_4$–($1-x$) $PbTiO_3$ films grown epitaxially on (001), (111), and (110) $SrTiO_3$ substrates with $x = 1/3$ and 2/3. The bright and dark regions correspond to $PbTiO_3$ and $CoFe_2O_4$, respectively. Reproduced from Ref. 25 by permission of © 2006 WILEY–VCH Verlag GmbH & Co. KGaA, Weinheim.

(110)- and (111)-oriented $SrTiO_3$ substrates, respectively, and then converts to irregular-shaped isolated columns of $PbTiO_3$ dispersed in a $CoFe_2O_4$ matrix and cylindrical $PbTiO_3$ nanorods in a $CoFe_2O_4$ matrix at $x = 2/3$. The evolution of morphologies is consistent with the results obtained from simulation of phase-field modeling, which describes that the equilibrium arrangements of phases are determined by minimizing the elastic and interfacial energies.[26] It also suggests that the strain energy between the two phases should be taken into account in addition to the surface energy in some of the self-assembled nanocomposite systems with higher structural coupling.

Besides, the use of different kinds of single-crystal substrates, of which the variation of lattice would cause disparity in surface energy, and also provides another means to tune the morphologies and crystallographic orientation of nanostructures. Liao et al. have used $(110)_o$-oriented $NdGaO_3$, $(001)_c$-oriented $SrTiO_3$, and $(110)_o$-oriented $DyScO_3$, where the pseudo-cubic and cubic lattice constants are $a_{pc} = 3.85$ Å, $a_c = 3.905$ Å, and $a_{pc} = 3.94$ Å, respectively (c, cubic; pc, pseudo-cubic; o, orthorhombic), to grow the self-assembled $BiFeO_3$ and $CoFe_2O_4$ VHN.[14] The sample on the (001)-oriented $SrTiO_3$ substrate exhibits the same results as the studies proposed by Zheng et al.[8,10] Interestingly, on the $(110)_o$-oriented [or $(001)_{pc}$-oriented] $DyScO_3$ and $NdGaO_3$ substrates, $BiFeO_3$ is still a matrix retaining the (001) orientation in the normal direction, but $CoFe_2O_4$ exhibits the morphologies of a roof-like islands with (110) orientation and triangle-platform islands with (111) orientation along the surface normal, respectively. These results imply that $CoFe_2O_4$ is more sensitive to the interface energy on different perovskite single-crystal substrates than $BiFeO_3$, and therefore, exhibits different morphologies and crystallographic orientations, whereas $BiFeO_3$ retains the same crystallographic orientation on these substrates.

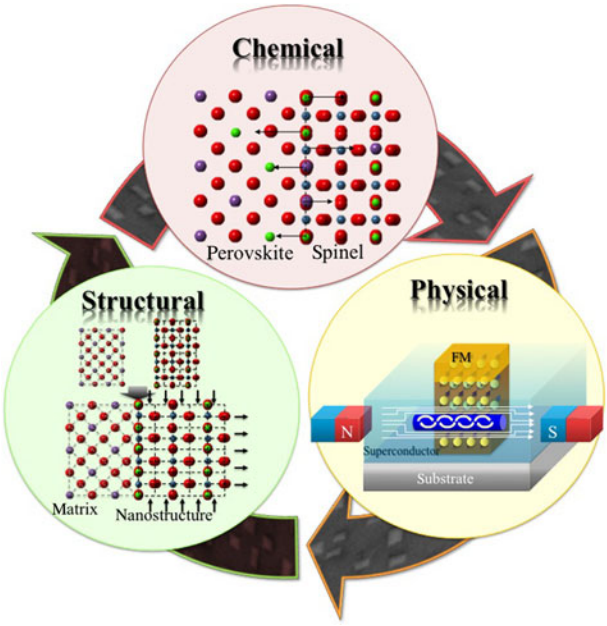


Figure 5. Schematic representation of the three main kinds of interactions happening correspondingly in VHN systems: the mechanical interaction via strain engineering; the physical interaction, such as superconductivity and ferromagnetism; and the chemical interaction by interdiffusion of elements.

Design of multi-functionalities

After having carefully reviewed the growth and control of VHN systems, we will now turn our attention to the various functionalities of VHN systems. In this part of the review, we shall discuss the three most important interactions, namely, mechanical, physical, and chemical, those lead to novel functionalities. Figure 5 illustrates the schematics of the three main interactions present in VHN systems.

Mechanical interaction

Mechanical effect is a derivative of thin-film strain engineering. In strongly correlated oxides, most of the properties are inherently connected to the crystalline structure and strain state; consequently, a subtle compromise of two connected lattices will change the physical properties of the resulting system. Traditionally, the strain state of thin-film heterostructure is determined by the type/nature of the substrate and film thickness. The strain state of the vertical self-assembled nanostructure, on the other hand, is majorly attributed to the lateral lattice mismatch between the pillar and matrix, which can thread through the entire structure, sustaining a stable strain state in the thick film.[27] The mechanical interaction plays a key role in tailoring the physical properties in VHN systems, such as the piezoelectricity–magnetostriction-induced ME

https://doi.org/10.1557/mrc.2014.13 Published online by Cambridge University Press

effect,[28–31] and photostriction–magnetostriction-induced photomagnetic effect.[15]

ME effect induced by elastic coupling

Single-phase multiferroics rely on the coupling of magnetic and electric orders resulting from spin–orbit interaction, which is usually weak, while composite MEs, the combination of magnetostrictive and electrostrictive materials, depend on the interfacial coupling interaction which can overpower the whole system under certain conditions. More so, vertical heterosturcture provides a clamping-free environment by virtue of its lateral geometry enhancing the net ferroelectricity in the system.[32–35] Theoretical calculations have also evidenced the extraordinary ME response since they possess long-range elastic interaction.[27,36–38] Therefore, VHN have become promising candidates to build ME response-based devices.

The emergence of VHN architecture has gained increased popularity in the field of oxide heterostructures since Ramesh's group[9] demonstrated the strong ME coupling by integrating ferroelectric $BaTiO_3$ perovskite and ferromagnetic $CoFe_2O_4$ spinel in the form of vertical nanostructures. Soon after this report, nanostructured composites aimed at multiferroic devices are widely studied with combinations of a number of room temperature ferroelectric perovskites [$PbTiO_3$,[39,40] Pb(Zr, Ti)O_3,[41–43] and $BiFeO_3$[44,45]] and room temperature ferromagnetic spinels ($CoFe_2O_4$,[39,40,42,43] $NiFe_2O_4$[41,44,45]). Of particular interest is the assembly of $BiFeO_3$–$CoFe_2O_4$ VHN system. From the structural aspect, $BiFeO_3$ and $CoFe_2O_4$ are compatible: $BiFeO_3$, with a pseudocubic lattice constant of 3.96 Å, is a room temperature multiferroic compound, exhibiting strong ferroelectric (100 μC/cm^2)[46,47] and antiferromagnetic behaviors, and $CoFe_2O_4$, with a cubic lattice constant of 8.38 Å, is a room temperature ferromagnet. From the chemistry aspect, bismuth and cobalt atoms with large differences in size and chemical properties scarcely react or mix. Hence, this system provides a simple yet decent model to study the kaleidoscope of ME coupling.

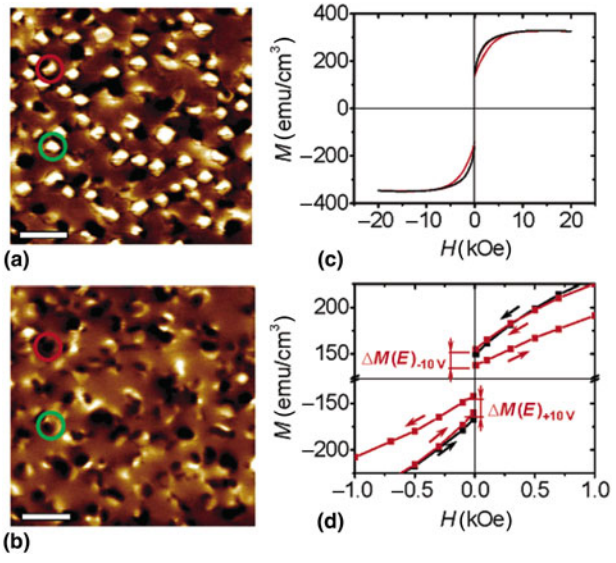


Figure 6. Changes in the magnetic response of a $(BiFeO_3)_{0.65}$–$(CoFe_2O_4)_{0.35}$ film upon electrical poling. Magnetic force microscopy image taken (a) after magnetization in an upward oriented 20 kOe perpendicular field, and (b) after electrical poling at +12 V along the out-of-plane direction (scale bars, 1 μm). (c) Magnetization measurement taken before (black curves), and after (red curves) electrical poling of 10% of the total film area. (d) Magnified view of M-H loop. Reprinted with permission from Ref. 36. © (2005) American Chemical Society.

Researchers have first grown epitaxial $BiFeO_3$–$CoFe_2O_4$ vertical heterostructures on $SrTiO_3$ substrate via PLD,[27] and with the help of scanning probe microscopy (SPM) technique, they have successfully demonstrated the magnetic switching behavior by electric field control (Fig. 6). The strength of ME coupling has been estimated to be $\sim 1.0 \times 10^{-2}$ G cm/V, whereas Yan et al. have directly measured the ME coefficient of ~20 mV/cm Oe by a magnetic cantilever method.[48] To inspect deeper, Oh et al.[49] have investigated the in-plane and out-of-plane ME susceptibilities (MES) separately by sensitive ME susceptometer equipped with PPMS. They have found that the in-plane MES is about 60 mV/cm Oe which behaves totally different in bulk materials. To apply the concept for practical applications, Zavaliche et al.[50] have found a way to control the selective magnetic configuration by applying the electric field in the $BiFeO_3$–$CoFe_2O_4$/$SrTiO_3$ system, and thus mapped out a comprehensive viewpoint for the working principle and controllability of electrically assisted magnetic recording via the SPM technique. Moreover, understanding the fundamentals and mechanism of ME coupling in the $BiFeO_3$–$CoFe_2O_4$/$SrTiO_3$ system has become an important issue. There has been tremendous effort, in terms of number of studies to decipher the detailed coupling behavior and mechanism. X-ray magnetic circular dichroism (XMCD) has directly observed the magnetic switching behavior of both Co and Fe in pillars after the electric poling.[51,52] This elasticity-induced ME coupling has been then directly proved via high-resolution transmission electron microscopy (HRTEM) and high-resolution x-ray diffraction (HRXRD).[53] Dynamics of switching behavior is another key to understand the nature of coupling. The observation of ferroic domain dynamics are recorded and revealed by piezoresponse force microscopy (PFM) and switching spectroscopy PFM (SS-PFM) (Fig. 7). They have conducted a systematic study at $BiFeO_3$, $CoFe_2O_4$, and $BiFeO_3$–$CoFe_2O_4$ interfaces and found that the switching and electrochemical responses are reduced in the vicinity of interface due to the long-range strain field. It indicates that the switching behavior is inert at the heterostructure interface.[54,55]

Photomagnetic effect

Besides the ME coupling, mechanically induced interaction has a considerable effect on some of the parameters/functionalities that are available to be part of system design. Another

https://doi.org/10.1557/mrc.2014.13 Published online by Cambridge University Press

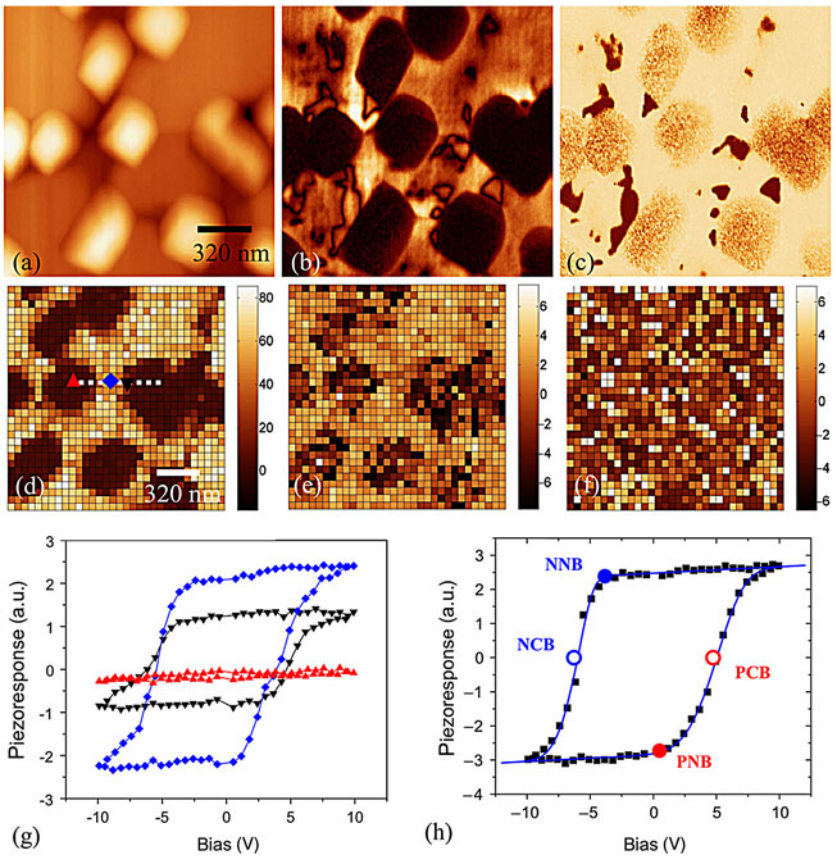


Figure 7. (a) Topography of multiferroic $BiFeO_3$–$CoFe_2O_4$ nanostructures and the corresponding PFM, (b) amplitude, and (c) phase images. The ferroelectric and antiferromagnetic $BiFeO_3$ show a piezoresponse, whereas the ferromagnetic $CoFe_2O_4$ spinels show no piezoresponse. (d) SS-PFM map of the work of switching and (e), (f) maps of the positive and negative nucleation biases, respectively. (g) Representative loops from $BiFeO_3$ (♦), $CoFe_2O_4$ (▲), and the $BiFeO_3$–$CoFe_2O_4$ heterostructure interface (▼). (h) Fit of the loop shape with coercive and nucleation biases indicated. The work of switching is defined as the area within a loop. Reproduced from Ref. 55 by permission of IOP Publishing. All rights reserved.

successful example is the combination of photostriction and magnetostriction in $SrRuO_3$–$CoFe_2O_4$ vertical heterostructure by Liu et al. in 2012.[15] In principle, photostriction can be understood as an effect coming from the superposition of photovoltage and the converse piezoelectricity, which has an intrinsic advantage for actuators or sensors applications in the ME noise-free system.[56,57] Lately, ultrafast XRD investigation of $SrRuO_3$ has revealed a large photon-induced strain of 0.5%–1.5% in a time scale of 500 fs laser-pulsed excitation.[58–61] Based on this discovery, the mechanical coupling between optical and magnetic parameters via the vertical heterostructure of $SrRuO_3$ and $CoFe_2O_4$ on the $SrTiO_3$ substrate has been demonstrated (Fig. 8). In the $SrRuO_3$–$CoFe_2O_4$/$SrTiO_3$ system, the magnetic anisotropy of $CoFe_2O_4$ is originally along the vertical direction of pillars; however, the femtosecond-pulsed laser excitation effectively extends the *c*-axis of $SrRuO_3$, partially relaxing the strain and therefore, the nearly isotropic magnetization results in the non-preferential magnetic domain direction at the same time. At this stage, the change of magnetic anisotropy permits $CoFe_2O_4$ magnetic domains to freely select orientation again. This work has introduced a novel approach to perturb magnetic moment orientation with light, which is also achieved by the interplay of epitaxial strain.

Physical interaction

Apart from mechanical coupling, there are parameters that interact physically. Explicit examples are phonon–electron coupling in $YBa_2Cu_3O_7$ and $La_{2/3}Ca_{1/3}MnO_3$ superlattice,[62,63] and superconductivity pinning effect in high-temperature superconductors (HTS) based two-phase materials system. Here, we will review some of the recent works on tailoring the functionalities like superconductivity through physical interaction.

Pinning engineering of superconductors

In 1986, the discovery of type-II HTS made superconductivity a popular research field for power applications.[64] However, an issue lies in that the magnetic flux partially retains in material as magnetic fluxons, hindering the supercurrents. Recently, researchers have dug out that the dense existence of pinning centers will largely enhance the critical current, and the approach to reach dense pinning centers is known as pinning engineering.[65–67] Several recent works on pinning

https://doi.org/10.1557/mrc.2014.13 Published online by Cambridge University Press

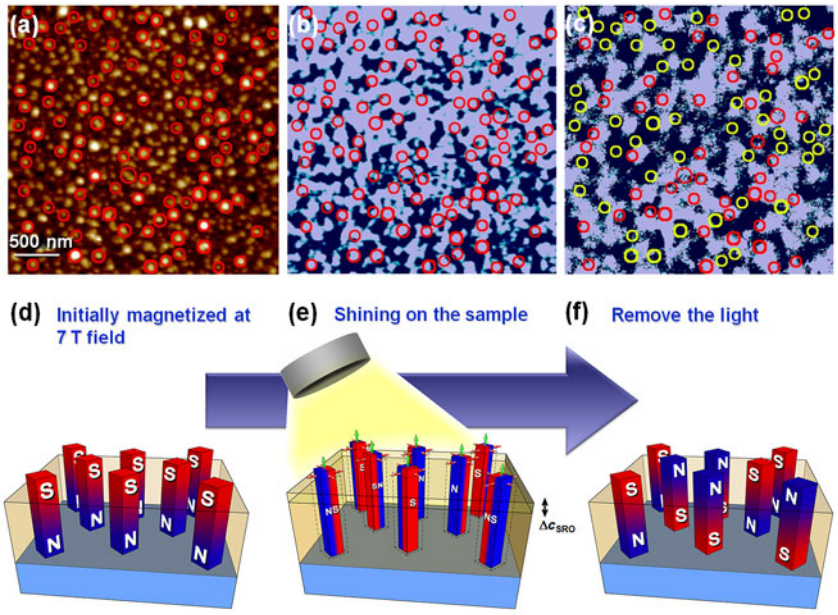


Figure 8. (a) AFM topology and (b) MFM image at the same area of a nanostructured $SrRuO_3$–$CoFe_2O_4$ sample magnetized by applying a large out-of-plane magnetic field before being illuminated. (c) MFM image at the same area after being illuminated. For convenience, randomly 100 nanopillars are selected to observe the change in magnetization direction. The red circles in (b) are the nanopillars in (a) with downward magnetization, and half of these pillars flipped upward in (c) are presented in yellow circles, suggesting a "liberation" in magnetization during illumination. (d)–(f) Schematic illustrations of the process of magnetic domain flipping during the illumination by ultrafast Ti:sapphire laser pulses—(d) Application of a large out-of-plane magnetic field (7 T) to magnetize all nanopillars downward. (e) Introduction of light on the nanostructured thin film expands the lattice of $SrRuO_3$ and releases the vertical compressive strain of $CoFe_2O_4$. (f) Removal of light results in the magnetization of the $CoFe_2O_4$ nanopillars to become either parallel or antiparallel to magnetic field direction for the energetically preferred state. Reprinted with permission from Ref. 15. © (2012) American Chemical Society.

engineering have been established parallel so far with the same goal for practical superconducting usage. For example, as shown in Figs. 9(a) and 9(b), Macmanus-Driscoll et al.[68] have started the work in 2004 by using structurally and chemically compatible nanoparticle $BaZrO_3$ as the pinning center in $YBa_2Cu_3O_7$ on single-crystal $SrTiO_3$ and $SrTiO_3$-buffered MgO substrate. $YBa_2Cu_3O_7$–$BaZrO_3$ samples of different thickness have been viewed and all the samples exhibit a huge enhancement in critical current density (J_c) over a wide magnetic field range (~1–5 T). In the same year, Haugan et al.[69] have synthesized YBa_2CuO_5 as second phase embedded in $YBa_2Cu_3O_7$ thin film to enhance J_c by a factor of 2. A fine columnar nanostructure of $BaZrO_3$ in $YBa_2Cu_3O_7$ thin film on biaxially textured substrates has also been carried out by Goyal et al.[70] Other than oxide-based superconductors, pinning engineering has also been investigated in ferropnictide superconductors. Eom's et al.[71] have successfully implanted vertically aligned second phase into $BaFe_2As_2$ via oxides template [Figs. 9(c)–9(e)]. With the aid of dense pinning sites along the *c*-axis, the irreversibility field (H_{irr}) anisotropy now can be inverted from the *a*–*b* plane to vertical plane. Furthermore, the same group consecutively gave a more sophisticated design of the artificial structure shown in Fig. 9(c),[72] which allows large as well as isotropic critical current behavior over a wide angular range. That is, these artificially controlled second phases in a superconductor film modify the functionalities that can be attributed to physical perturbation rather than mechanical or chemical effect.

Chemical interaction

Diffusion, which is a representative for mass transportation, is a phenomenon ubiquitously known/existed in the dissimilar-component system.[73] Generally speaking, it is well established that elemental mixing engenders a wide range of modifications depending on the basic properties of host and doped atoms. Chemical interaction discussed in this report infers that the interaction between disparate ions from two distinctive oxides happens in heterostructures, which is based on interdiffusion. It is especially important in strongly correlated systems since the ions strongly interacts with electrons and thereof couples with physical properties.[74,75]

ME coupling induced by chemistry

ME coupling, as discussed earlier, has been on a huge demand in the development of the next generation electronics. However, improvements are often limited by the choices of ferroelectric and ferromagnetic oxides system. Very recently, Liang et al.[76] have discovered a large ME effect in ferroelectric/antiferromagnetic vertical heterostructure by means of chemical interaction. They have manipulated the vertical heterostructure of $BiFeO_3$–$LiMn_2O_4$ with different concentration ratio to control the degree of Fe doping in $LiMn_2O_4$. According to the study, the

https://doi.org/10.1557/mrc.2014.13 Published online by Cambridge University Press

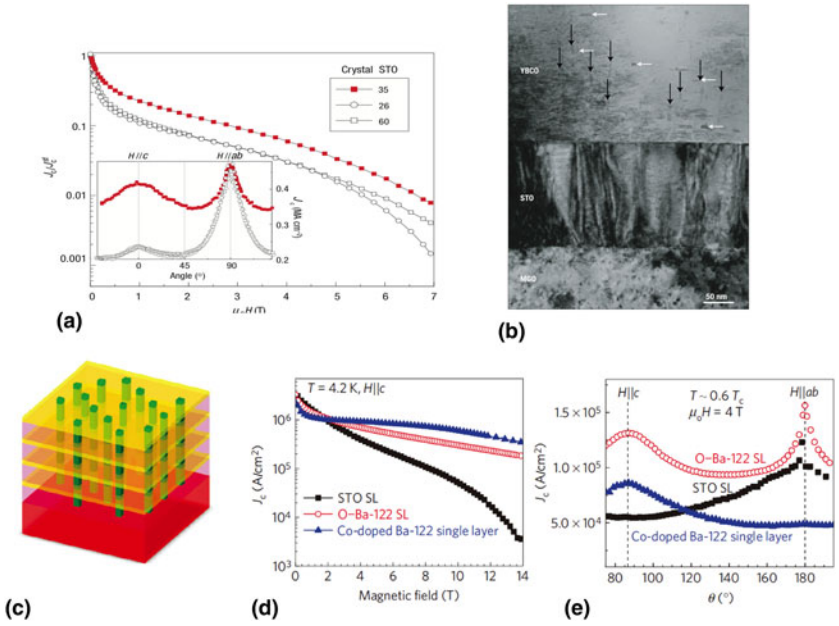


Figure 9. (a) The example for superconductor with nanoparticle structure; the critical current density measured parallel to *c*-axis for pure $YBa_2Cu_3O_7$ (black) and $YBa_2Cu_3O_7 + BaZrO_3$ films (red). (b) The TEM images showing nanoparticle embedded in $YBa_2Cu_3O_7$ film. (c) is the illustration for the superlattice structure with defects along the *c*-axis. (d) and (e) are examples for the structure shown in (c); critical current density for $SrTiO_3$ SL [in black, representing ($SrTiO_{3\,1.2\,nm}$/co-doped $Ba122_{13\,nm}$) × ($n = 24$) superlattice], O–Ba-122 SL [in red, (O–$Ba\text{-}122_{3\,nm}$/co-doped $Ba122_{13\,nm}$) × ($n = 24$) superlattice] and co-doped Ba-122 single layer (in blue). (e) shows the angular dependence of critical current density at 4 T. (a) and (b) are reprinted from Ref. 68, copyright (2004) and (c)–(e) from Ref. 72, copyright (2013) by permission from Macmillan Publishers Ltd: [Nature Materials].

substitution of Fe for Mn induces the net spin in $LiMn_2O_4$,[77] and it has been evidenced by SPM, Auger, and XMCD that in the $(BiFeO_3)_{0.66}$–$(LiMn_2O_4)_{0.37}$ system ferroelectricity and ferromagnetism coexist below room temperature [Fig. 10(a)]. ME coupling based on chemical interaction rather than elastic strain is demonstrated by variable field module [Figs. 10(b)–10(d)]. This study gives a decent example for creating new functionality by playing materials chemistry.

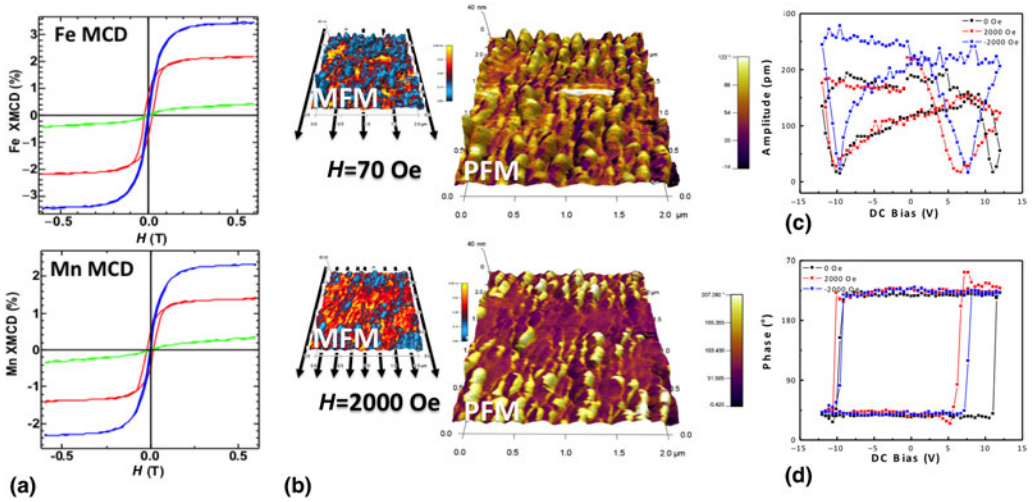


Figure 10. (a) The chemical evidence for spin coupling between Mn and Fe ions by XMCD measurement. (b) The ME coupling is measured by variable field module with different magnetic field. The ferroelectric switching response on the application of magnetic field is facilitated as shown in (c) phase hysteresis and (d) amplitude loop. Reproduced from Ref. 76 by permission of the Royal Society of Chemistry.

https://doi.org/10.1557/mrc.2014.13 Published online by Cambridge University Press

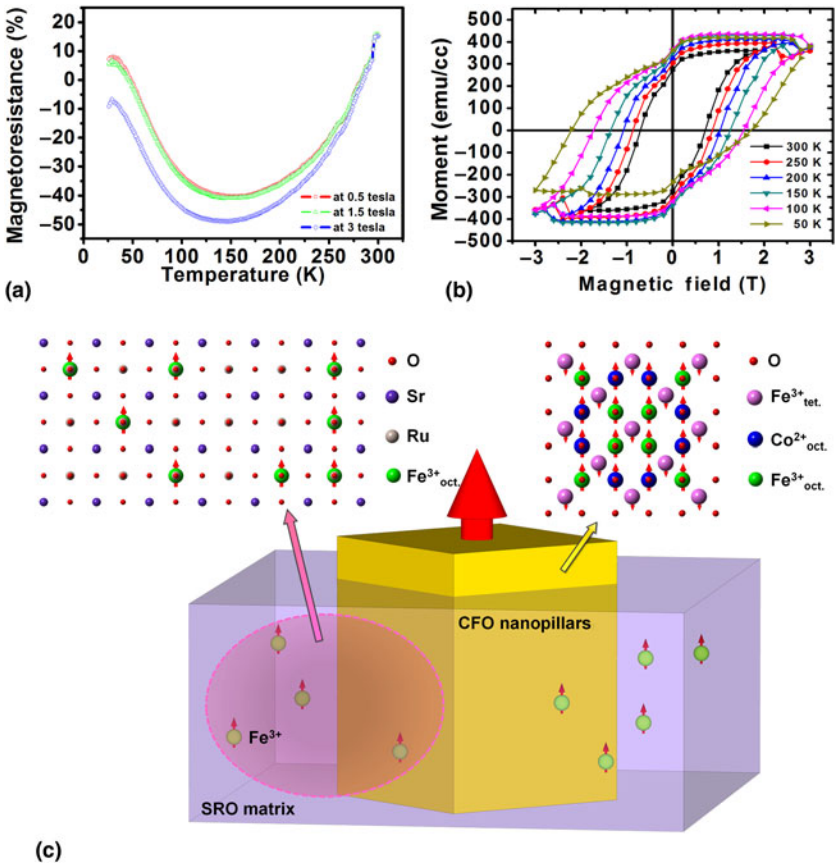


Figure 11. (a) The respective MR at 0.5, 1.5, and 3 T exhibit a ~40% decrease of resistivity about 150 K (Curie temperature of $SrRuO_3$). (b) The hysteresis loops measured at different temperatures show an obviously decoupled feature below $T_{C,SrRuO3}$. (c). The depiction of the cause of large MR in this nanostructure system. The interdiffused Fe ions and $CoFe_2O_4$ nanopillars play a role to reduce the resistivity while they are put in a magnetic field. The aligned magnetic moments of Fe ions in $SrRuO_3$ matrix and $CoFe_2O_4$ nanopillars result in the suppression of magnetic scattering from ions and interfaces. Reproduced from Ref. 84 by permission of © 2013 WILEY–VCH Verlag GmbH & Co. KGaA, Weinheim.

MR effect

MR effect, which gave the birth of a new spintronic era, has become a large playground in quantum physics and solid-state physics for decades. Significant MR are usually found in the mixed valence perovskite manganite system with spin polarization in 3d orbitals, described by the double-exchange mechanism.[78] However, the MR effect in single-phase perovskite manganite is observed only in high magnetic field (H = several Tesla).[79,80] To meet the criteria for practical applications, some works have pointed out that grain boundary in polycrystalline manganite induces spin tunneling and results in the enhancement of MR in relatively low magnetic field ($H <$ 1 T).[11,81–83] Taking advantage of heterostructure that includes uniform artificial grain boundary, Liu et al.[84] have obtained an unexpectedly large MR effect in VHN with two non-manganite-based oxides, which is later confirmed resulting from atomic diffusion. As shown in Fig. 11, $SrRuO_3$–$CoFe_2O_4$ VHN is demonstrated and they have found that it shows a significant 40% decrease of resistivity in 0.5 T magnetic field about 150 K (Curie temperature of $SrRuO_3$). Authors have pointed out that the key to this abnormal MR is the Fe^{3+} diffusion, which makes this nanocomposite system present a strong magnetic coupling. A model is also proposed in Fig. 11(c).

Outlook

So far, many investigations have already pointed out the fantastic physical properties and desired multifunctionalities in the self-assembled VHN films; however, some further directions are still needed to be carried out. First, the creation of various multifunctionalities by coupling of two or more constituent materials may be the faster and more efficient direction than looking for the single-phase materials with the same effect. To understand how many multifunctionalities can be created in self-assembled nanocomposites, we start with five commonly observed intrinsic properties of materials, such as permittivity/conductivity, permeability, elastic constant, specific heat capacity, and optical indices. The corresponding input sources to manipulate these properties are electric field, magnetic field, stress, heat, and light.[85] By cross-linking these

https://doi.org/10.1557/mrc.2014.13 Published online by Cambridge University Press

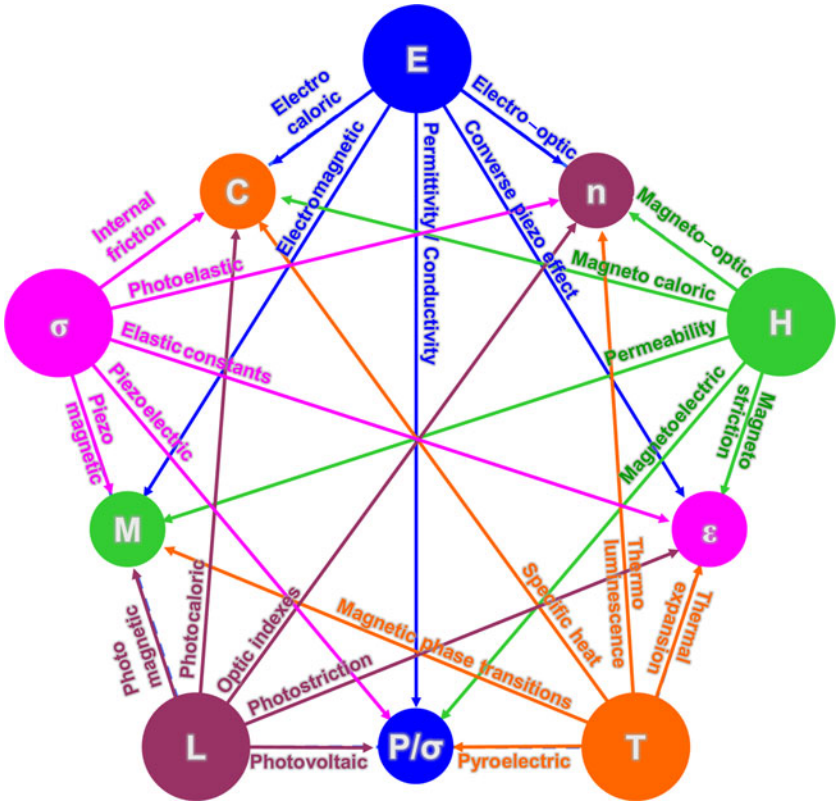


Figure 12. Obtainable functionalities by cross-linking of the input sources (big circles) with controllable physical properties (small circles). Five commonly available input sources: *E*, electric field; *H*, magnetic field; *T*, heat; *L*, light or electromagnetic wave; and σ, stress. The corresponding physical properties: P/ρ, permittivity/resistivity; *M*, permeability; *C*, specific heat; *n*, optic indexes; and ϵ, elastic constants. The so-called "multifunctionalities" means the intrinsic physical properties can be operated by other kinds of input sources.

input sources with other controllable properties, the so-called "multifunctionalities" can be obtained as shown in Fig. 12. From this figure, we can find that in addition to the ME effect, photomagnetic effect, and large MR mentioned earlier, it seems that many "intelligent" functions are still being discovered in self-assembled nanocomposite systems through correct design and fabrication.

Second, most of the investigations about the self-assembled VHN films are mainly constructed on the oxides-based systems, for example, perovskites-spinels and perovskites-wurtzites. Different types of oxides can usually have strong structural compatibility with others through the bridge of oxygen atoms, and thus they are easier to form heterointerfaces when interconnected. Interactions across heterointerfaces sometimes carry unusual properties that are definitely worth studying for fundamental understanding, for example, the electrically modulated local conduction at tubular interfaces around the nanopillars in $BiFeO_3$–$CoFe_2O_4$ system.[86] Although oxides have a very broad range of applications, they still have some limitations on physical properties such as electric conductivity, compared to those non-oxides systems. An attempt to grow the self-assembled nanocomposites films combining metals or semiconductors with oxides may be another feasible direction in this field of research for higher practicality. Vidal et al. have successfully demonstrated that the deposition of co-doped CeO_2 under special growth condition leads to the reduction of CoO into slanted Co nanowires assembly embedded in $CeO_2/SrTiO_3$ (001) epilayers. The sample exhibits interesting magneto-optical properties with rather strong values of the Faraday ellipticity.[87,88] This is a good instance to confirm the possibility of self-assembled VHN films composed of oxides and non-oxides. Such combinations will extend the self-assembled VHN films into a brand-new area and create more chances for special purposes.

Apart from the scientific investigations, there are some impediments that hinder the realization for practical applications. One is the stochastic distribution of $CoFe_2O_4$ pillars in $BiFeO_3$–$CoFe_2O_4$ vertical heterostructure. The self-assembled VHN films with ordered arrangement of nanostructures hold great promise for novel applications such as microelectronics, optoelectronics, photonics, and energy storage. How to make nanopillars in controllable and periodic arrangement is an important issue. Currently, using a patterned substrate or pretreated template such as anodic aluminum oxide (AAO) to create a preferred nucleation site for the formation of nanostructures seems to be the way[89,90] A recent work has overcome

https://doi.org/10.1557/mrc.2014.13 Published online by Cambridge University Press

the distribution issue intriguingly with the control of lithography patterning method by assistance of focused ion beam (FIB).[88] The results indeed show a nicely ordered array of $BiFeO_3$–$CoFe_2O_4$ vertical heterostructure with high degree control of nanopillar density, which facilitates the future device development. However, the process is arduous to make a large patterned area and takes great effort for preliminary preparation. From this viewpoint, integrating VHN thin film with industrial chain still needs phenomenal breakthrough in the future. Although several concepts have been proposed to functionalize $BiFeO_3$–$CoFe_2O_4$ for working devices,[50,91] the real demonstration is still in urgent need so far.

In VHN architecture, the freedom of growth controllability and functional versatility makes it fascinating and glamorous. Undiscovered phenomena, design of creative functionalities, and industrialization are expected to come up in the near future, leading to scientific contributions and novel applications for the next generation devices.

Acknowledgments

This work was supported by the National Science Council, Republic of China (NSC-101-2119-M-009-003-MY2), Ministry of Education (MOE-ATU 101W961), and Center for Interdisciplinary Science of National Chiao Tung University.

References

1. J.L. MacManus-Driscoll: Self-assembled heteroepitaxial oxide nanocomposite thin film structures: designing interface-induced functionality in electronic materials. *Adv. Funct. Mater.* **20**, 2035 (2010).
2. C.-W. Nan, M.I. Bichurin, S. Dong, D. Viehland, and G. Srinivasan: Multiferroic magnetoelectric composites: historical perspective, status, and future directions. *J. Appl. Phys.* **103**, 031101 (2008).
3. R. Ramesh and N.A. Spaldin: Multiferroics: progress and prospects in thin films. *Nat. Mater.* **6**, 21 (2007).
4. D.G. Schlom, L.-Q. Chen, X. Pan, A. Schmehl, and M.A. Zurbuchen: A thin film approach to engineering functionality into oxides. *J. Am. Ceram. Soc.* **91**, 2429 (2008).
5. R.E. Newnham and S. Trolier-McKinstry: Crystals and composites. *J. Appl. Crystallogr.* **23**, 447 (1990).
6. O.I. Lebedev, J. Verbeeck, G. Van Tendeloo, O. Shapoval, A. Belenchuk, V. Moshnyaga, B. Damashcke, and K. Samwer: Structural phase transitions and stress accommodation in $(La_{0.67}Ca_{0.33}MnO_3)_{1-x}$:$(MgO)_x$ composite films. *Phys. Rev. B* **66**, 104421 (2002).
7. V. Moshnyaga, B. Damaschke, O. Shapoval, A. Belenchuk, J. Faupel, O.I. Lebedev, J. Verbeeck, G. van Tendeloo, M. Mucksch, V. Tsurkan, R. Tidecks, and K. Samwer: Structural phase transition at the percolation threshold in epitaxial $(La_{0.7}Ca_{0.3}MnO_3)_{1-x}$:$(MgO)_x$ nanocomposite films. *Nat. Mater.* **2**, 247 (2003).
8. H. Zheng, F. Straub, Q. Zhan, P.L. Yang, W.K. Hsieh, F. Zavaliche, Y.-H. Chu, U. Dahmen, and R. Ramesh: Self-assembled growth of $BiFeO_3$–$CoFe_2O_4$ nanostructures. *Adv. Mater.* **18**, 2747 (2006).
9. H. Zheng, J. Wang, S.E. Lofland, Z. Ma, L. Mohaddes-Ardabili, T. Zhao, L. Salamanca-Riba, S.R. Shinde, S.B. Ogale, F. Bai, D. Viehland, Y. Jia, D.G. Schlom, M. Wuttig, A. Roytburd, and R. Ramesh: Multiferroic $BaTiO_3$–$CoFe_2O_4$ nanostructures. *Science* **303**, 661 (2004).
10. H. Zheng, Q. Zhan, F. Zavaliche, M. Sherburne, F. Straub, M.P. Cruz, L.-Q. Chen, U. Dahmen, and R. Ramesh: Controlling self-assembled Perovskite-spinel nanostructures. *Nano Lett.* **6**, 1401 (2006).
11. A. Chen, Z. Bi, C.-F. Tsai, J. Lee, Q. Su, X. Zhang, Q. Jia, J.L. MacManus-Driscoll, and H. Wang: Tunable low-field magnetoresistance in $(La_{0.7}Sr_{0.3}MnO_3)_{0.5}$:$(ZnO)_{0.5}$ self-assembled vertically aligned nanocomposite thin films. *Adv. Funct. Mater.* **21**, 2423 (2011).
12. H. Yang, H. Wang, J. Yoon, Y. Wang, M. Jain, D.M. Feldmann, P.C. Dowden, J.L. MacManus-Driscoll, and Q. Jia: Vertical interface effect on the physical properties of self-assembled nanocomposite epitaxial films. *Adv. Mater.* **21**, 3794 (2009).
13. A. HarringtonSophie, J. Zhai, S. Denev, V. Gopalan, H. Wang, Z. Bi, A.T. RedfernSimon, S.-H. Baek, C.W. Bark, C.-B. Eom, Q. Jia, M.E. Vickers, and J.L. MacManus-Driscoll: Thick lead-free ferroelectric films with high Curie temperatures through nanocomposite-induced strain. *Nat. Nano* **6**, 491 (2011).
14. S.-C. Liao, P.-Y. Tsai, C.-W. Liang, H.-J. Liu, J.-C. Yang, S.-J. Lin, C.-H. Lai, and Y.-H. Chu: Misorientation control and functionality design of nanopillars in self-assembled Perovskite – Spinel heteroepitaxial nanostructures. *ACS Nano* **5**, 4118 (2011).
15. H.-J. Liu, L.-Y. Chen, Q. He, C.-W. Liang, Y.-Z. Chen, Y.-S. Chien, Y.-H. Hsieh, S.-J. Lin, E. Arenholz, C.-W. Luo, Y.-L. Chueh, Y.-C. Chen, and Y.-H. Chu: Epitaxial photostriction–magnetostriction coupled self-assembled nanostructures. *ACS Nano* **6**, 6952 (2012).
16. N.M. Aimon, D.H. Kim, H.K. Choi, and C.A. Ross: Deposition of epitaxial $BiFeO_3$/$CoFe_2O_4$ nanocomposites on (001) $SrTiO_3$ by combinatorial pulsed laser deposition. *Appl. Phys. Lett.* **100**, 092901 (2012).
17. R. Comes, M. Khokhlov, H. Liu, J. Lu, and S.A. Wolf: Magnetic anisotropy in composite $CoFe_2O_4$–$BiFeO_3$ ultrathin films grown by pulsed-electron deposition. *J. Appl. Phys.* **111**, 07D914 (2012).
18. M. Staruch, D. Hires, A. Chen, Z. Bi, H. Wang, and M. Jain: Enhanced low-field magnetoresistance in $La_{0.67}Sr_{0.33}MnO_3$:MgO composite films. *J. Appl. Phys.* **110**, 113913 (2011).
19. Y.-H. Hsieh, H.-H. Kuo, S.-C. Liao, H.-J. Liu, Y.-J. Chen, H.-J. Lin, C.-T. Chen, C.-H. Lai, Q. Zhan, Y.-L. Chueh, and Y.-H. Chu: Tuning the formation and functionalities of ultrafine $CoFe_2O_4$ nanocrystals *via* interfacial coherent strain. *Nanoscale* **5**, 6219 (2013).
20. D. Wu: Nucleation theory. *Solid State Phys.* **50**, 37 (1996).
21. G. Srinivasan, E.T. Rasmussen, J. Gallegos, R. Srinivasan, Y.I. Bokhan, and V.M. Laletin: Magnetoelectric bilayer and multilayer structures of magnetostrictive and piezoelectric oxides. *Phys. Rev. B* **64**, 214408 (2001).
22. L. Yan, F. Bai, J. Li, and D. Viehland: Nanostructures in perovskite–ferrite two-phase composite epitaxial thin films. *Phil. Mag.* **90**, 103 (2009).
23. L. Yan, Y. Yang, Z. Wang, Z. Xing, J. Li, and D. Viehland: Review of magnetoelectric perovskite–spinel self-assembled nano-composite thin films. *J. Mater. Sci.* **44**, 5080 (2009).
24. I. Stern, J. He, X. Zhou, P. Silwal, L. Miao, J.M. Vargas, L. Spinu, and D.H. Kim: Role of spinel substrate in the morphology of $BiFeO_3$–$CoFe_2O_4$ epitaxial nanocomposite films. *Appl. Phys. Lett.* **99**, 082908 (2011).
25. I. Levin, J. Li, J. Slutsker, and A.L. Roytburd: Design of self-assembled multiferroic nanostructures in epitaxial films. *Adv. Mater.* **18**, 2044 (2006).
26. A. Artemev, J. Slutsker, and A.L. Roytburd: Phase field modeling of self-assembling nanostructures in constrained films. *Acta Mater.* **53**, 3425 (2005).
27. J.L. MacManus-Driscoll, P. Zerrer, H. Wang, H. Yang, J. Yoon, A. Fouchet, R. Yu, M.G. Blamire, and Q. Jia: Strain control and spontaneous phase ordering in vertical nanocomposite heteroepitaxial thin films. *Nat. Mater.* **7**, 314 (2008).
28. N. Mathur: Materials science: a desirable wind up. *Nature* **454**, 591 (2008).
29. C.-W. Nan, G. Liu, Y. Lin, and H. Chen: Magnetic-field-induced electric polarization in multiferroic nanostructures. *Phys. Rev. Lett.* **94**, 197203 (2005).
30. Y. Wang, J. Hu, Y. Lin, and C.-W. Nan: Multiferroic magnetoelectric composite nanostructures. *NPG Asia Mater.* **2**, 61 (2010).
31. K.H. Sun and Y.Y. Kim: Design of magnetoelectric multiferroic heterostructures by topology optimization. *J. Phys. D: Appl. Phys.* **44**, 185003 (2011).
32. G. Caruntu, A. Yourdkhani, M. Vopsaroiu, and G. Srinivasan: Probing the local strain-mediated magnetoelectric coupling in multiferroic nanocomposites by magnetic field-assisted piezoresponse force microscopy. *Nanoscale* **4**, 3218 (2012).

https://doi.org/10.1557/mrc.2014.13 Published online by Cambridge University Press

33. S.Q. Ren, L.Q. Weng, S.H. Song, F. Li, J.G. Wan, and M. Zeng: $BaTiO_3$/$CoFe_2O_4$ particulate composites with large high frequency magnetoelectric response. *J. Mater. Sci.* **40**, 4375 (2005).
34. M.V. Ramanaa, N.R. Reddy, G. Sreenivasulu, K.V.S. Kumar, B.S. Murty, and V.R.K. Murthy: Enhanced mangnetoelectric voltage in multiferroic particulate $Ni_{0.83}Co_{0.15}Cu_{0.02}Fe_{1.9}O_{4-\delta}$/$PbZr_{0.52}Ti_{0.48}O_3$ composites—dielectric, piezoelectric and magnetic properties. *Curr. Appl. Phys.* **9**, 1134 (2009).
35. D. Wu, W. Gong, H. Deng, and M. Li: Magnetoelectric composite ceramics of nickel ferrite and lead zirconate titanate *via* in situ processing. *J. Phys. D: Appl. Phys.* **40**, 5002 (2007).
36. F. Zavaliche, H. Zheng, L. Mohaddes-Ardabili, S.Y. Yang, Q. Zhan, P. Shafer, E. Reilly, R. Chopdekar, Y. Jia, P. Wright, D.G. Schlom, Y. Suzuki, and R. Ramesh: Electric field-induced magnetization switching in epitaxial columnar nanostructures. *Nano Lett.* **5**, 1793 (2005).
37. J. Slutsker, I. Levin, J. Li, A. Artemev, and A.L. Roytburd: Effect of elastic interactions on the self-assembly of multiferroic nanostructures in epitaxial films. *Phys. Rev. B* **73**, 184127 (2006).
38. L.D. Landau and E.M. Liftshitz: *Electrodynamics of Continuous Media* (Pergamon Press, Oxford, 119, 1960).
39. J. Li, I. Levin, J. Slutsker, V. Provenzano, P.K. Schenck, R. Ramesh, J. Ouyang, and A.L. Roytburd: Self-assembled multiferroic nanostructures in the $CoFe_2O_4$–$PbTiO_3$ system. *Appl. Phys. Lett.* **87**, 072909 (2005).
40. C.Y. Tsai, H.R. Chen, F.C. Chang, W.C. Tsai, H.M. Cheng, Y.-H. Chu, C. H. Lai, and W.F. Hsieh: Stress-mediated magnetic anisotropy and magnetoelastic coupling in epitaxial multiferroic $PbTiO_3$–$CoFe_2O_4$ nanostructures. *Appl. Phys. Lett.* **102**, 132905 (2013).
41. S. Ren and M. Wuttig: Spinodally synthesized magnetoelectric. *Appl. Phys. Lett.* **91**, 083501 (2007).
42. J.G. Wan, X.W. Wang, Y.J. Wu, M. Zeng, Y. Wang, H. Jiang, W.Q. Zhou, G.H. Wang, and J.-M. Liu: Magnetoelectric $CoFe_2O_4$–$Pb(Zr,Ti)O_3$ composite thin films derived by a sol–gel process. *Appl. Phys. Lett.* **86**, 122501 (2005).
43. J. Zhang, H. Fu, W. Lu, J. Dai, and H.L.W. Chan: Nanoscale free-standing magnetoelectric heteropillars. *Nanoscale* **5**, 6747 (2013).
44. S.P. Crane, C. Bihler, M.S. Brandt, S.T.B. Goennenwein, M. Gajek, and R. Ramesh: Tuning magnetic properties of magnetoelectric $BiFeO_3$–$NiFe_2O_4$ nanostructures. *J. Magn. Magn. Mater.* **321**, L5 (2009).
45. Q. Zhan, R. Yu, S.P. Crane, H. Zheng, C. Kisielowski, and R. Ramesh: Structure and interface chemistry of perovskite–spinel nanocomposite thin films. *Appl. Phys. Lett.* **89**, 172902 (2006).
46. Y.-H. Chu, Q. Zhan, L.W. Martin, M.P. Cruz, P.L. Yang, G.W. Pabst, F. Zavaliche, S.Y. Yang, J.X. Zhang, L.Q. Chen, D.G. Schlom, I.N. Lin, T.B. Wu, and R. Ramesh: Nanoscale domain control in multiferroic $BiFeO_3$ thin films. *Adv. Mater.* **18**, 2307 (2006).
47. G.W. Pabst, L.W. Martin, Y.-H. Chu, and R. Ramesh: Leakage mechanisms in $BiFeO_3$ thin films. *Appl. Phys. Lett.* **90**, 072902 (2007).
48. L. Yan, Z. Xing, Z. Wang, T. Wang, G. Lei, J. Li, and D. Viehland: Direct measurement of magnetoelectric exchange in self-assembled epitaxial $BiFeO_3$–$CoFe_2O_4$ nanocomposite thin films. *Appl. Phys. Lett.* **94**, 192902 (2009).
49. Y.S. Oh, S. Crane, H. Zheng, Y.-H. Chu, R. Ramesh, and K.H. Kim: Quantitative determination of anisotropic magnetoelectric coupling in $BiFeO_3$–$CoFe_2O_4$ nanostructures. *Appl. Phys. Lett.* **97**, 052902 (2010).
50. F. Zavaliche, T. Zhao, H. Zheng, F. Straub, M.P. Cruz, P.L. Yang, D. Hao, and R. Ramesh: Electrically assisted magnetic recording in multiferroic nanostructures. *Nano Lett.* **7**, 1586 (2007).
51. T. Zhao, A. Scholl, F. Zavaliche, H. Zheng, M. Barry, A. Doran, K. Lee, M. P. Cruz, and R. Ramesh: Nanoscale x-ray magnetic circular dichroism probing of electric-field-induced magnetic switching in multiferroic nanostructures. *Appl. Phys. Lett.* **90**, 123104 (2007).
52. Y.-J. Chen, Y.-H. Hsieh, S.-C. Liao, Z. Hu, M.-J. Huang, W.-C. Kuo, Y.-Y. Chin, T.-M. Uen, J.-Y. Juang, C.-H. Lai, H.-J. Lin, C.-T. Chen, and Y.-H. Chu: Strong magnetic enhancement in self-assembled multiferroic-ferrimagnetic nanostructures. *Nanoscale* **5**, 4449 (2013).
53. N. Dix, R. Muralidharan, J. Guyonnet, B. Warot-Fonrose, M. Varela, P. Paruch, F. Sánchez, and J. Fontcuberta: On the strain coupling across vertical interfaces of switchable $BiFeO_3$–$CoFe_2O_4$ multiferroic nanostructures. *Appl. Phys. Lett.* **95**, 062907 (2009).
54. S.V. Kalinin, A.N. Morozovska, L.Q. Chen, and B.J. Rodriguez: Local polarization dynamics in ferroelectric materials. *Rep. Prog. Phys.* **73**, 056502 (2010).
55. B.J. Rodriguez, S. Jesse, A.P. Baddorf, T. Zhao, Y.-H. Chu, R. Ramesh, E.A. Eliseev, A.N. Morozovska, and S.V. Kalinin: Spatially resolved mapping of ferroelectric switching behavior in self-assembled multiferroic nanostructures: strain, size, and interface effects. *Nanotechnology* **18**, 405701 (2007).
56. P. Poosanaas, K. Tonooka, and K. Uchino: Photostrictive actuators. *Mechatronics* **10**, 467 (2000).
57. K. Uchino and M. Aizawa: Photostrictive actuator using PLZT ceramics. *Japan. J. Appl. Phys.* **24S3**, 139 (1985).
58. C.v.K. Schmising, M. Bargheer, M. Kiel, N. Zhavoronkov, M. Woerner, T. Elsaesser, I. Vrejoiu, D. Hesse, and M. Alexe: Strain propagation in nanolayered perovskites probed by ultrafast x-ray diffraction. *Phys. Rev. B* **73**, 212202 (2006).
59. C.v.K. Schmising, M. Bargheer, M. Kiel, N. Zhavoronkov, M. Woerner, T. Elsaesser, I. Vrejoiu, D. Hesse, and M. Alexe: Coupled ultrafast lattice and polarization dynamics in ferroelectric nanolayers. *Phys. Rev. Lett.* **98**, 257601 (2007).
60. C.v.K. Schmising, A. Harpoeth, N. Zhavoronkov, Z. Ansari, C. Aku-Leh, M. Woerner, T. Elsaesser, M. Bargheer, M. Schmidbauer, I. Vrejoiu, D. Hesse, and M. Alexe: Ultrafast magnetostriction and phonon-mediated stress in a photoexcited ferromagnet. *Phys. Rev. B* **78**, 060404R (2008).
61. C.v.K. Schmising, M. Bargheer, M. Kiel, N. Zhavoronkov, M. Woerner, T. Elsaesser, I. Vrejoiu, D. Hesse, and M. Alexe: Ultrafast structure and polarization dynamics in nanolayered perovskites studied by femtosecond X-ray diffraction. *J. Phys.: Conf. Ser.* **92**, 012177 (2007).
62. N. Driza, S. Blanco-Canosa, M. Bakr, S. Soltan, M. Khalid, L. Mustafa, K. Kawashima, G. Christiani, H.U. Habermeier, G. Khaliullin, C. Ulrich, M. Le Tacon, and B. Keimer: Long-range transfer of electron–phonon coupling in oxide superlattices. *Nat. Mater.* **11**, 675 (2012).
63. S. Heinze, H.-U. Habermeier, G. Cristiani, S.B. Canosa, M.L. Tacon, and B. Keimer: Thermoelectric properties of $YBa_2Cu_3O_{7-\delta}$–$La_{2/3}Ca_{1/3}MnO_3$ superlattices. *Appl. Phys. Lett.* **101**, 131603 (2012).
64. J.G. Bednorz and K.A. Müller: Possible high T_C superconductivity in the Ba—La—Cu—O system. *Z. Phys. B: Condens. Matter* **64**, 189 (1986).
65. D. Larbalestier, A. Gurevich, D.M. Feldmann, and A. Polyanskii: High-T_C superconducting materials for electric power applications. *Nature* **414**, 368 (2001).
66. B. Dam, J.M. Huijbregtse, F.C. Klaassen, R.C.F. van der Geest, G. Doornbos, J.H. Rector, A.M. Testa, S. Freisem, J.C. Martinez, B. Stauble-Pumpin, and R. Griessen: Origin of high critical currents in $YBa_2Cu_3O_{7-\delta}$ superconducting thin films. *Nature* **399**, 439 (1999).
67. T. Matsushita: Flux pinning in superconducting 123 materials. *Supercond. Sci. Technol.* **13**, 730 (2000).
68. J.L. MacManus-Driscoll, S.R. Foltyn, Q.X. Jia, H. Wang, A. Serquis, L. Civale, B. Maiorov, M.E. Hawley, M.P. Maley, and D.E. Peterson: Strongly enhanced current densities in superconducting coated conductors of $YBa_2Cu_3O_{7-x}$ + $BaZrO_3$. *Nat. Mater.* **3**, 439 (2004).
69. T. Haugan, P.N. Barnes, R. Wheeler, F. Meisenkothen, and M. Sumption: Addition of nanoparticle dispersions to enhance flux pinning of the $YBa_2Cu_3O_{7-x}$ superconductor. *Nature* **430**, 867 (2004).
70. A. Goyal, S. Kang, K.J. Leonard, P.M. Martine, A.A. Gapud, M. Varela, M. Paranthaman, A.O. Ijaduola, E.D. Specht, j.R. Thompson, D. K. Chrhten, S.J. Pennycook, and F.A. List: Irradiation-free, columnar defects comprised of self-assembled nanodots and nanorods resulting in strongly enhanced flux-pinning in $YBa_2Cu_3O_{7-\delta}$ films. *Supercond. Sci. Technol.* **18**, 1533 (2005).
71. S. Lee, J. Jiang, Y. Zhang, C.W. Bark, J.D. Weiss, C. Tarantini, C.T. Nelson, H.W. Jang, C.M. Folkman, S.H. Baek, A. Polyanskii, D. Abraimov, A. Yamamoto, J.W. Park, X.Q. Pan, E.E. Hellstrom, D.C. Larbalestier, and C.B. Eom: Template engineering of co-doped $BaFe_2As_2$ single-crystal thin films. *Nat. Mater.* **9**, 397 (2010).
72. S. Lee, C. Tarantini, P. Gao, J. Jiang, J.D. Weiss, F. Kametani, C.M. Folkman, Y. Zhang, X.Q. Pan, E.E. Hellstrom, D.C. Larbalestier, and C.B. Eom: Artificially engineered superlattices of pnictide superconductors. *Nat. Mater.* **12**, 392 (2013).

https://doi.org/10.1557/mrc.2014.13 Published online by Cambridge University Press

73. W.D.J. Callister: *Materials Science and Engineering: An Introduction*, 7th ed. (Wiley, 2006) p. 110,129.
74. E. Dagotto: Complexity in strongly correlated electronic systems. *Science* **309**, 257 (2005).
75. J. Mannhart and D.G. Schlom: Oxide interfaces—an opportunity for electronics. *Science* **327**, 1607 (2010).
76. W.-I. Liang, Y. Liu, S.-C. Liao, W.-C. Wang, H.-J. Liu, H.-J. Lin, C.-T. Chen, C.-H. Lai, A. Borisevich, E. Arenholz, J. Li, and Y.-H. Chu: Design magnetoelectric coupling in a self-assembled epitaxial nanocomposite *via* chemical interaction. *J. Mater. Chem. C*, **2**, 811 (2014)
77. P.P. Hankare, R.P. Patil, U.B. Sankpal, S.D. Jadhav, I.S. Mulla, K. M. Jadhav, and B.K. Chougule: Magnetic and dielectric properties of nanophase manganese-substituted lithium ferrite. *J. Magn. Magn. Mater.* **321**, 3270 (2009).
78. C. Zener: Interaction between the d shells in the transition metals. *Phys. Rev.* **81**, 440 (1951).
79. S. Jin, T.H. Tiefel, M. McCormack, R.A. Fastnacht, R. Ramesh, and L.H. Chen: Thousandfold change in resistivity in magnetoresistive La–Ca–Mn–O films. *Science* **264**, 413 (1994).
80. G.J. Snyder, R. Hiskes, S. DiCarolis, M.R. Beasley, and T.H. Geballe: Intrinsic electrical transport and magnetic properties of $La_{0.67}Ca_{0.33}MnO_3$ and $La_{0.67}Sr_{0.33}MnO_3$ MOCVD thin films and bulk material. *Phys. Rev. B* **53**, 14434 (1996).
81. R. Gross, L. Alff, B. Büchner, B.H. Freitag, C. Höfener, J. Klein, Y. Lu, W. Mader, J.B. Philipp, M.S.R. Rao, P. Reutler, S. Ritter, S. Thienhaus, S. Uhlenbruck, and B. Wiedenhorst: Physics of grain boundaries in the colossal magnetoresistance manganites. *J. Magn. Magn. Mater.* **211**, 150 (2000).
82. Y.H. Huang, M. Karppinen, H. Yamauchi, and J.B. Goodenough: Effect of high-pressure annealing on magnetoresistance in manganese perovskites. *J. Appl. Phys.* **98**, 033911 (2005).
83. H.Y. Hwang, S.W. Cheong, N.P. Ong, and B. Batlogg: Spin-polarized intergrain tunneling in $La_{2/3}Sr_{1/3}MnO_3$. *Phys. Rev. Lett.* **77**, 2041 (1996).
84. H.-J. Liu, V.-T. Tra, Y.-J. Chen, R. Huang, C.-G. Duan, Y.-H. Hsieh, H.-J. Lin, J.-Y. Lin, C.-T. Chen, Y. Ikuhara, and Y.-H. Chu: Large magnetoresistance in magnetically coupled $SrRuO_3$–$CoFe_2O_4$ self-assembled nanostructures. *Adv. Mater.* **25**, 4753 (2013).
85. V.V. Pokropivny and V.V. Skorokhod: New dimensionality classifications of nanostructures. *Physica E* **40**, 2521 (2008).
86. Y.-H. Hsieh, J.-M. Liou, B.-C. Huang, C.-W. Liang, Q. He, Q. Zhan, Y.-P. Chiu, Y.-C. Chen, and Y.-H. Chu: Local conduction at the $BiFeO_3$–$CoFe_2O_4$ tubular oxide interface. *Adv. Mater.* **24**, 4564 (2012).
87. F. Vidal, P. Schio, N. Keller, Y. Zheng, D. Demaille, F.J. Bonilla, J. Milano, and A.J.A. de Oliveira: Magneto-optical study of slanted Co nanowires embedded in CeO_2/$SrTiO_3$(0 01). *Physica B* **407**, 3070 (2012).
88. F. Vidal, Y. Zheng, J. Milano, D. Demaille, P. Schio, E. Fonda, and B. Vodungbo: Nanowires formation and the origin of ferromagnetism in a diluted magnetic oxide. *Appl. Phys. Lett.* **95**, 152510 (2009).
89. R. Comes, H. Liu, M. Khokhlov, R. Kasica, J. Lu, and S.A. Wolf: Directed self-assembly of epitaxial $CoFe_2O_4$–$BiFeO_3$ multiferroic nanocomposites. *Nano Lett.* **12**, 2367 (2012).
90. W. Lee, H. Han, A. Lotnyk, M.A. Schubert, S. Senz, M. Alexe, D. Hesse, S. Baik, and U. Gösele: Individually addressable epitaxial ferroelectric nanocapacitor arrays with near Tb $inch^{-2}$ density. *Nat. Nanotechnol.* **3**, 402 (2008).
91. S.A. Wolf, L. Jiwei, M.R. Stan, E. Chen, and D.M. Treger: The promise of nanomagnetics and spintronics for future logic and universal memory. *Proc. IEEE* **98**, 2155 (2010).

https://doi.org/10.1557/mrc.2014.13 Published online by Cambridge University Press